

# Scalable parallel measurement of individual nitrogen-vacancy centers

Matthew Cambria<sup>1</sup>, Saroj Chand<sup>1</sup>, Shimon Kolkowitz<sup>1,2,\*</sup>

<sup>1</sup>Department of Physics, University of California, Berkeley, CA, USA

<sup>2</sup>Department of Physics, University of Wisconsin, Madison, WI, USA

\*Corresponding author(s). E-mail(s): kolkowitz@berkeley.edu;

## Abstract

The nitrogen-vacancy (NV) center in diamond is a solid-state spin defect that has been widely adopted for quantum sensing<sup>1,2</sup> and quantum information processing applications<sup>3,4</sup>. Typically, experiments are performed either with a single isolated NV center or with an unresolved ensemble of many NV centers, resulting in a trade-off between measurement speed and spatial resolution or control over individual defects. In this work, we introduce an experimental platform that bypasses this trade-off by addressing multiple optically resolved NV centers in parallel. We perform charge- and spin-state manipulations selectively on multiple NV centers from within a larger set, and we manipulate and measure the electronic spin states of 10 NV centers in parallel. Further, we show that the high signal-to-noise ratio of the measurements enables the detection of shot-to-shot pairwise correlations between the spin states of 10 NV centers, corresponding to the simultaneous measurement of 45 unique correlation coefficients. We conclude by discussing how our platform can be scaled to parallel experiments with thousands of individually resolved NV centers. These results

**enable high-throughput experiments with individual spin defects, and provide a natural platform for the application of recently developed correlated sensing techniques<sup>5-8</sup>.**

The nitrogen-vacancy (NV) center in diamond has emerged as a solid-state platform with applications in quantum sensing<sup>9-11</sup> and quantum information processing<sup>12,13</sup>. The NV center is notable for its robust and optically accessible electronic spin ground-state, which can exhibit coherence times of several milliseconds at room temperature<sup>14,15</sup>. As a result, the NV center is now a versatile quantum sensor with applications in condensed matter physics<sup>16-18</sup>, biology<sup>19,20</sup>, and chemistry<sup>21,22</sup>. Almost all experiments with NV centers are performed either by interrogating one spatially resolved NV center at a time or by interrogating ensembles of many unresolved NV centers. Measurements with single NV centers offer nanoscale spatial resolution, but are typically slow, requiring many repetitions of an experiment to average down shot noise, and only provide information about the local environment at one spatial location at a time<sup>23,24</sup>. Measurements with ensembles of many NV centers can be comparatively fast, but their spatial resolution is limited by optical diffraction, and information is lost in the process of averaging over the ensemble<sup>25,26</sup>. In particular, wide-field implementations in which a dense 2D layer of NV centers is imaged onto a camera have become an important tool in quantum sensing<sup>27</sup>, but are not suitable for applications that require readout and control at the level of individual NV centers.

Several recent works have developed a new measurement modality in which shot-to-shot correlations between signals from several NV centers are used to obtain information about the environment which is otherwise difficult to access<sup>5-8</sup>. These correlated sensing techniques require both the ability to work with multiple NV centers simultaneously, and the ability to associate an experimental signal with a specific NV center. In Ref. [5], correlations between the spin states of two optically resolved NV centers were measured using a confocal microscope modified with a 50:50 beamsplitter to allow for independent addressing and readout of each NV. Because half the light from each NV is lost and each NV requires its

own lasers and photodetector, the scalability of this approach is limited. The techniques developed in Refs. [6–8] are designed to measure correlations between NV centers within a single diffraction-limited spot, and require that the NV centers in the spot have frequency-resolved optical<sup>6,7</sup> or microwave<sup>8</sup> transitions.

Motivated by these considerations, in this work we present an experimental platform for the simultaneous parallel interrogation of multiple spatially resolved NV centers in a scalable manner. Our approach is inspired by recent advances in neutral atom tweezer arrays<sup>28</sup>, and makes use of NV center-selective charge-state manipulations and wide-field single-shot charge-state readout with an electron-multiplying CCD (EMCCD) camera to conduct parallel charge- and spin-state experiments with high signal-to-noise ratios. We demonstrate the ability to measure pairwise correlations between NV center spin states, and the ability to deterministically initialize a group of NV centers into the  $NV^-$  charge state using conditional logic. We anticipate that these results will aid in the scaling up of quantum sensing and quantum information processing applications with NV centers as well as with other spin defects.

## Platform for parallel measurement

Experiments are conducted using 13 NV centers from a 2D layer of NV centers within a bulk diamond sample (Fig. 1a). The experimental apparatus is illustrated in Fig. 1b. The experiments described in this work are conducted under ambient conditions. However, our approach could readily be integrated into a cryostat for low temperature experiments. Charge-state manipulation and histograms of integrated photon counts from single-shot charge-state readout for a single NV center selected from within the camera images are shown in Fig. 1c. The NV center is prepared in  $NV^-$  with over 75% probability by a 520-nm charge-polarization pulse, and the charge state can be subsequently read out in a single shot with the camera under 589-nm illumination (green histogram). The two well-resolved

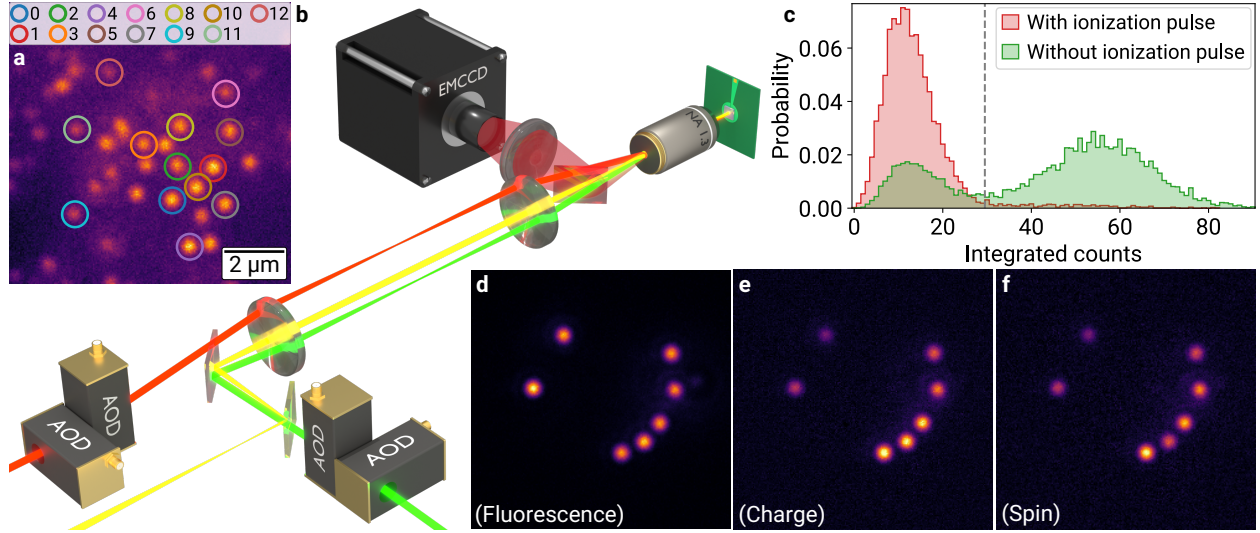


**Fig. 1 | Experimental platform.** **a**, Wide-field image under 589-nm illumination with index of the 13 NV centers addressed in this work. **b**, Illustration of the experimental apparatus. The 589-nm laser beam is focused at the back aperture of the objective to attain a spot size of roughly 20 microns at the objective focal plane, while the 520-nm and 638-nm lasers fill the back aperture of the objective and are focused to diffraction-limited spots in the objective focal plane. By switching the frequencies of the drive tones applied to the AODs, we are able to rapidly reposition the 520-nm and 638-nm laser beams between target NV centers (within 10  $\mu$ s). A microwave antenna<sup>29</sup> delivers global microwave pulses. NV centers are imaged onto an EMCCD camera. **c**, Charge-state manipulation and readout. The histograms show the probability of recording a given number of photons from a single NV center in a 50 ms exposure after polarization into  $NV^-$  (green) and  $NV^0$  (red). The grey dashed line shows the threshold used for charge-state determination. **d-f**, “Smiley face” pattern made up of seven single NV centers written in fluorescence, charge, and spin. The images show the same region as in panel (a). In panel (d), the NV centers are imaged directly under targeted 520-nm illumination. Panel (e) shows the average difference between images recorded after preparation into the  $NV^-$  and  $NV^0$  charge states. Panel (f) shows the average difference between images recorded preparation into the  $m_s = -1$  and  $m_s = 0$  spin states, following spin-to-charge conversion (SCC).

histogram modes correspond to the NV charge states and allow for single-shot charge-state readout by thresholding<sup>30</sup>. Alternatively, the NV center can be prepared in  $NV^0$  with an additional 638-nm ionization pulse applied after the initial 520-nm charge-polarization pulse (red histogram).

By repositioning the 520-nm and 638-nm beams we are able to selectively target a subset of NV centers with minimal crosstalk affecting nearby NV centers. We demonstrate this capability by generating a “smiley face” pattern out of a subset of seven NV centers in three

distinct ways (Fig. 1d-f). In Fig. 1d, the pattern is drawn in fluorescence by targeting the seven NV centers in series with 520-nm illumination while continuously exposing the camera. In Fig. 1e, the pattern is written into the charge states of the seven NV centers. The panel shows the average difference between pairs of images recorded under 589-nm illumination following preparation of the selected centers in  $NV^-$  ( $NV^0$ ) for the first (second) image of each pair. The pattern is written into the spin states of the seven NV centers in a similar manner in Fig. 1f. Here, after charge polarization the NV centers are prepared in the  $m_s = 0$  spin state by a global 589-nm spin polarization pulse<sup>31</sup>. A microwave  $\pi$  pulse flips the NV spins to the  $m_s = -1$  state for the first image of each pair, whereas no  $\pi$  pulse is applied for the second image. Before readout, a 638-nm spin-to-charge conversion (SCC) pulse<sup>32</sup> is applied in series to each NV center.

## Conditional charge-state initialization

We next leverage non-destructive parallel charge-state readout and NV center-selective optical pulses in order to achieve high-fidelity charge-state initialization of multiple NV centers simultaneously. By repeatedly interrogating the charge states of a group of NV centers and re-initializing only those that are found in  $NV^0$ , the group can be deterministically prepared in  $NV^-$ . This scheme is demonstrated with 10 NV centers in Fig. 2a, where on average over 9 NV centers are found in  $NV^-$  after three initialization attempts. In contrast, on average 7.7 NV centers are found in  $NV^-$  in the unconditional initialization case (green dashed line), where before each readout all NV centers are initialized with 520-nm illumination. Example camera single-shot images are shown in fig. 2b. In the third panel, after three initialization attempts all 10 NV centers were found in  $NV^-$ , representing an instance of “defect-free” charge-state initialization of a set of NV centers analogous to the generation of defect-free arrays of neutral atoms via imaging and conditional rearrangement<sup>33-35</sup>.

We note that a 100 ms exposure was used to achieve non-destructive single-shot charge-

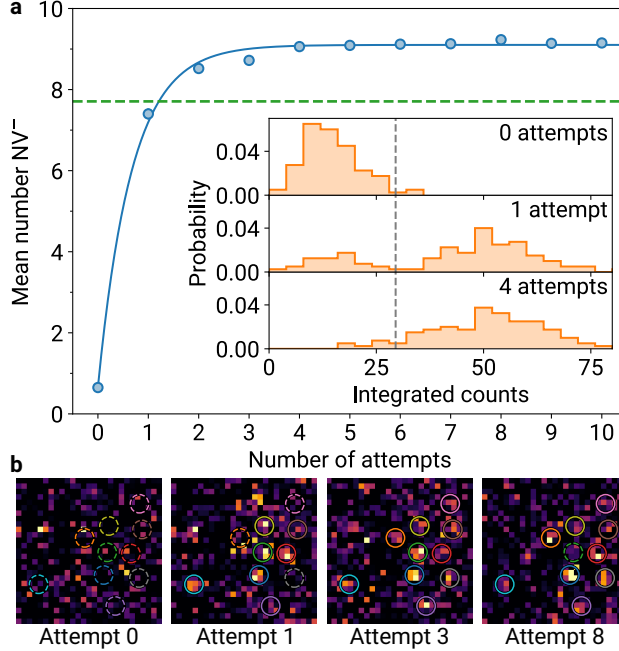


**Fig. 2 | Deterministic initialization of 10 NV centers into NV<sup>-</sup> with conditional logic.** **a**, Scaling of mean number of NV centers in NV<sup>-</sup> with number of conditional initialization attempts. The NV centers are polarized into NV<sup>0</sup> at the beginning of each experimental run. After charge-state readout, NV centers found in NV<sup>0</sup> are re-initialized with 520-nm charge-polarization pulses, and this process of charge-state readout and conditional initialization is repeated. Error bars (one standard error) are smaller than the data points. The data is fit to an analytical model (blue curve) described in the Methods section. The green dashed line shows the mean number of NV centers found in NV<sup>-</sup> after unconditional initialization. Inset: Evolution of photon count histograms with number of initialization attempts for a single NV center. The grey dashed line shows the threshold. **b**, Example single-shot images from the experimental data shown in panel (a). The images are background-subtracted and downsampled by a factor of 6 along each axis. The background is the average image recorded after polarizing the 10 NV centers into NV<sup>0</sup>. Each NV center used in the experiment is circled with a dashed or solid line according to whether the NV was found in NV<sup>0</sup> or NV<sup>-</sup> respectively.

state readout for the experiments shown in Fig. 2. The experiments described throughout the rest of this work use a 50 ms exposure and a higher 589 nm intensity. While conditional initialization involves a large measurement time overhead, it can still offer improved efficiency over unconditional initialization in certain cases, such as correlated sensing with higher-order joint cumulants<sup>5</sup> or experiments with long interrogation times. In the Outlook section we discuss prospects for reducing the duration of non-destructive charge-state readout, which will broaden the range of experiments where conditional initialization is beneficial. For the

experiments described in the remainder of this work we initialize unconditionally.

## Parallel high-fidelity spin experiments

Our platform enables independent experiments with multiple spins to be conducted in parallel. Using the experimental sequence shown in Fig. 3a, we perform parallel pulsed electron spin resonance (ESR) and spin echo measurements with 10 NV centers. Fig. 3b shows the

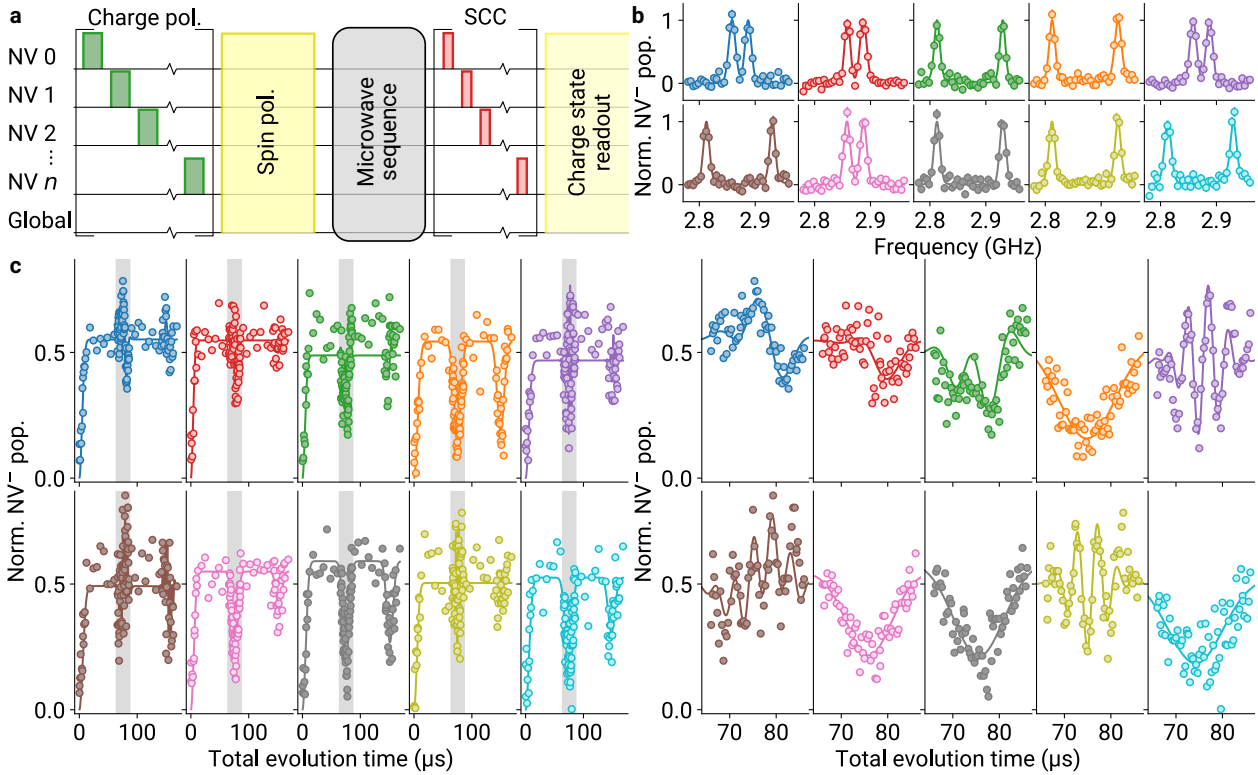


**Fig. 3 | Parallel spin measurements with 10 NV centers.** **a**, Experimental sequence. The green, yellow, and red blocks indicate illumination with 520 nm, 589 nm, and 638 nm respectively. The global microwave sequence (grey block) varies depending on the experiment. Charge polarization and SCC steps are conducted by applying optical pulses to the  $n$  NV centers in series. **b**, Parallel pulsed electron spin resonance (ESR) experiments. Experiments are conducted on 10 NV centers indexed 0-9 in Fig. 1a.  $\text{NV}^-$  populations are normalized such that 0 (1) corresponds to the  $\text{NV}^-$  population measured after preparation in  $m_s = 0$  ( $m_s = -1$ ). Error bars (one standard error) are smaller than the data points. **c**, Parallel spin echo experiments. Left and right sets of plots show the same data and fits, with the first revival in coherence (gray shaded region) detailed in the right set of plots. Error bars are omitted for clarity. See Methods for fit details .

resonance frequencies of each NV center’s  $m_s = 0 \leftrightarrow m_s = \pm 1$  transitions, as measured with pulsed ESR. Two of the possible four orientations of NV centers are represented. While all four orientations of NV centers are present in our diamond sample, the polarization of the 589-nm light used for charge-state readout is only well-aligned with the optical dipole moments of two orientations. NV centers of the misaligned orientations are dim under 589-nm illumination and so are not used here (Methods). In Fig. 3c, parallel spin echo reveals details about all 10 NV centers’ local environments simultaneously. Oscillations in the revivals of spin coherence (at around 75 and 150  $\mu\text{s}$ ) indicate the presence of strongly coupled C13 nuclei for 6 out of 10 of the targeted NV centers. The oscillation frequencies can be used to determine the locations of the  $^{13}\text{C}$  nuclei with respect to the NV center<sup>36</sup>, providing a proof-of-principle example of nanoscale NMR performed with multiple NV centers simultaneously. More sophisticated pulse sequences could be used to detect dozens of nuclear spins coupled to each NV center in parallel<sup>37,38</sup>, and even to perform operations on multiple small-scale quantum registers in parallel<sup>3</sup>. With current parameters our platform provides a speedup over fully serial measurements conducted with conventional spin readout using 532-nm illumination for experiments with just 10 NV centers for an interrogation time of 100  $\mu\text{s}$ . For experiments with 100 NV centers and the same interrogation and readout times, our platform would offer an order-of-magnitude speedup over the serial approach (Methods).

## Pairwise shot-to-shot spin correlations

Our platform also allows for the detection of classical shot-to-shot pairwise correlations across all targeted NV center spins<sup>5</sup>. The experimental sequence we use to generate and measure correlations is shown in Fig. 4a. Following charge and spin polarization, a microwave  $\pi$  pulse is randomly either applied or not applied from shot to shot, setting up positive correlations between the spin states of all 10 NV centers. Negative correlations can then be introduced by inserting an additional  $\pi$  pulse within the serialized SCC step.



We first conduct the correlation measurement sequence with no microwave pulses applied (Fig. 4b). Ideally, there would be no shot-to-shot correlations in this case. In practice, fluctuations in laser intensities, sample drift, and noise sources affecting the EMCCD camera all introduce background correlations. The mean background correlation level we measure is  $0.0015 \pm 0.0027$  (one standard deviation). Upon introduction of the randomly applied

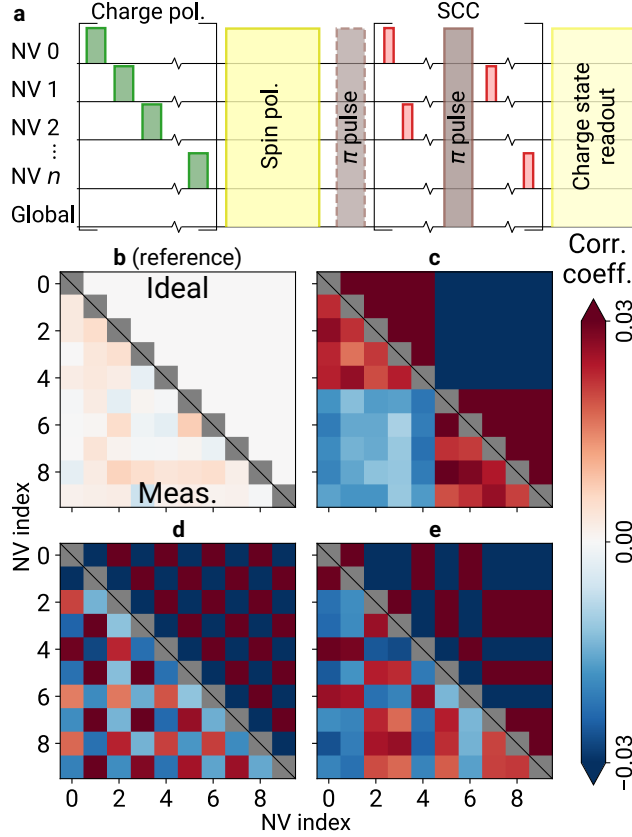


**Fig. 4 | Pairwise correlations between spin states of 10 NV centers.** **a**, Example experimental sequence. Each brown block indicates a pair of microwave  $\pi$  pulses addressing the two orientations of NV centers under study. The dashed  $\pi$  pulse block is applied randomly from shot to shot. **b-e**, Correlation matrices for “reference” (b), “block” (c), “checkerboard” (d), and “orientation” (e) experiments. The upper and lower triangular sections of each matrix show the ideal and measured results respectively. The diagonal elements, which are equal to 1 by definition, are shown in grey. (b) No microwaves are applied. (c) An additional  $\pi$  pulse is inserted between the SCC pulses for NV centers 0-4 and 5-9, generating a block pattern. (d) SCC pulses are rearranged and an additional  $\pi$  pulse is inserted as in the sequence shown in panel (a) above, generating a checkerboard pattern. (e) Before SCC, an additional  $\pi$  pulse is applied for only one orientation such that NV centers with the same (different) orientations are positively (negatively) correlated.

$\pi$  pulse, we measure correlations with a mean absolute value of  $0.0210 \pm 0.0053$ , an order of magnitude larger than the background level. We note that in most covariance sensing applications quantum projection noise will decrease the contrast of the measured correlations by a factor of 2 relative to the induced correlations measured here. Fig. 4c-e show three different experiments where the SCC step of the sequence is modified to generate different patterns in the correlation matrix. Each experimentally measured correlation matrix mirrors the ideal expected matrix.

The results presented in Fig. 4 demonstrate that our platform meets three important requirements for practical covariance magnetometry with NV centers<sup>5</sup>. First, high-fidelity single-NV measurements are required, as the amount of time needed to resolve a correlated signal scales with the fourth power of the readout noise of a single NV center<sup>5</sup>, rather than with the square of the readout noise as in the case of non-correlated measurements<sup>39</sup>. Second, the number of correlation coefficients probed in a single experiment scales combinatorially with the number of NV centers measured simultaneously. Practical covariance magnetometry therefore benefits from parallel operation of many sensors in order to probe a range of correlation lengths, rather than measuring one two-point correlation function at a time. Finally, our ability to generate arbitrary pairwise anticorrelations by flipping a subset of NV spins prior to readout can be used to isolate spin correlations by canceling out common-mode contributions from background technical correlations<sup>5</sup>.

## Outlook

We have demonstrated parallel control and measurement of the electronic spin states of 10 individual NV centers simultaneously. The number of NV centers addressed simultaneously was primarily limited by background fluorescence during charge-state readout. Background fluorescence impacts the duration of the exposure required to achieve single-shot charge state readout, and thereby affects total measurement time. Background fluorescence can be

mitigated by restricting the wide-field illumination spot size at the expense of field of view. In this work we opted for an approximately 20  $\mu\text{m}$  spot size to balance these competing interests, limiting us to roughly 10 NV centers with the two preferred orientations given the density of NV centers in the diamond sample and the readout times and target fidelities used here. Reduced background fluorescence could be achieved without sacrificing field of view by using an array of focused illumination spots generated by a digital micromirror device (DMD) or spatial light modulator (SLM). Alternatively, illumination with a light sheet would eliminate background from out-of-focus sources<sup>40</sup>. As we anticipate that most of the background fluorescence we observe originates from out-of-focus NV centers at other depths within the diamond, a delta-doped high-purity diamond sample could offer the same benefits as a light sheet without requiring modifications to the experimental apparatus<sup>41</sup>.

With reduced background fluorescence, we expect the scalability of our approach to become limited by the spin lifetimes of the NV centers. At room temperature, the spin state relaxes on millisecond time scales for NV centers deep in bulk diamond<sup>42</sup>, and shorter time scales for shallow NV centers<sup>43,44</sup> and NV centers in nanodiamonds<sup>45</sup>. Given the access times of the AODs used in this work, around 500 NV centers could be addressed in series within the  $1/e$  time constant for spin contrast at room temperature (Methods). Faster AOD operation could allow for parallel experiments with over 1,000 NV centers at room temperature. At cryogenic temperatures, where the NV spin lifetime can exceed 10 seconds<sup>46</sup>, we anticipate that scalability will be limited by the angular bandwidth of the AODs. In this regime we estimate that parallel measurements with over 9,000 NV centers should be achievable (Methods). Measurements performed at cryogenic temperatures could also take advantage of single-shot spin-state readout techniques to further enhance the signal-to-noise ratio and enable conditional spin-state preparation<sup>47–49</sup>.

The results presented here demonstrate scalable control over individual solid-state spin defects. Our platform can be used for the application of correlated sensing techniques to condensed matter systems<sup>50</sup>, and will increase measurement throughput in applications where

parallelization could prove critical, such as single molecule NMR<sup>51</sup> and quantum simulation with nuclear spin registers<sup>52,53</sup>.

**Authors' note:** We are aware of a manuscript that describes complementary work performed in parallel to our own in which multiplexing of measurements with individual NV centers in diamond is demonstrated<sup>54</sup>. Both works deploy low readout noise cameras to measure many NV centers simultaneously; in Ref. [54], Cheng *et al.* make use of a spatial light modulator rather than acousto-optic deflectors as a complementary alternative addressing technology.

## Data availability

All data related to this study are available from the corresponding author upon request.

## Code availability

All code used for data analysis related to this study is available from the corresponding author upon request.

## Acknowledgements

We thank Carter Fox for contributions to the early stages of the experiment, and Kevin Villegas for suggestions regarding the experimental sequences. We acknowledge helpful conversations with Jared Rovny, Jeff Thompson, Kai-Hung Cheng, Zeeshawn Kazi, and Nathalie de Leon. Design and construction of the experimental apparatus, as well as work on parallel ESR and spin echo measurements, was supported by the U.S. Department of Energy Office of Science National Quantum Information Science Research Centers as part of the Q-NEXT center. Work on high fidelity charge state readout and conditional charge state initialization was supported by the U.S. Department of Energy, Office of Science, Basic Energy Sciences under Award No. DE-SC0020313. Work on parallel shot-to-shot correlation measurements

was supported by the NSF under Award No. 2326767.

## Author contributions

S.K. conceived the experimental platform. M.C. and S.C. constructed the apparatus. M.C. performed the experiments and analysed the data. S.K. supervised the research. M.C. and S.K. wrote the paper with input from S.C.

## Competing interests

The authors declare no competing interests.

## Methods

### Experimental details

The EMCCD camera used in this work is a Nüvü HNü 512 Gamma with a resolution of  $512 \times 512$  pixels. A region of interest of  $512 \times 200$  pixels is used to reduce the camera readout duration. A Quantum Machines OPX is used for experimental sequencing, including conditional logic and AOD drive tone generation. The AODs used in this work are Brimrose 2DS series. The microscope objective is an Olympus MPLAPON100XO2 oil objective with a numerical aperture of 1.45. A permanent magnet is used to lift the degeneracy between the  $m_s = \pm 1$  spin states and allow for microwave frequency resolution of NV centers of different orientations.

**Diamond sample.** The diamond sample used in this work is from Element Six and was grown by chemical-vapor-deposition. The NV centers in the sample were formed naturally during growth. The sample displays an inhomogeneous concentration of NV centers with different areas exhibiting concentrations between  $10^{-5}$  and  $10^{-3}$  ppb, as estimated by direct counting. The higher-concentration regions are localized in irregularly-spaced layers that are

nearly two-dimensional relative to the microscope depth of field. The NV centers studied in this work are from the second such plane from the surface, about 15  $\mu\text{m}$  down. The NV centers in this plane allow for the highest fidelity single-shot charge-state readout. Aberrations associated with the high index of refraction of diamond diminishes readout fidelity for NV centers in planes further from the surface. A slight (roughly 10%) increase in background fluorescence diminishes readout fidelity for the NV centers in the first plane from the surface, about 5  $\mu\text{m}$  down.

**Optical pulse parameters.** 520-nm charge polarization pulses are 1  $\mu\text{s}$  at 5 mW. 638-nm ionization pulses are 1  $\mu\text{s}$  at 5 mW. 638-nm SCC pulses are optimized in both duration and power on a per NV basis, but are 100–132 ns at 9–10 mW. 589-nm spin polarization pulses are 10  $\mu\text{s}$  at 0.3 mW. 589-nm charge-state readout pulses are 50 ms at 0.2 mW (for Figs. **1**, **3**, and **4** of the main text) or 100 ms at 0.1 mW (for Fig. **2** of the main text).

**Number of shots and experimental run times.** Here we describe the averaging statistics for the data sets shown in Figs. **3** and **4** of the main text. The duration for a single shot in each of the experiments shown in Figs. **3** and **4** of the main text is dominated by the 50 ms exposure for readout. There is a 12 ms dead time between shots as the image is read off the EMCCD pixel array, and an additional overhead of approximately 10% associated with drift tracking. Each point in the ESR data shown in Fig. **3b** of the main text is the average of 2000 shots, and there are 40 data points in total. Each point in the spin echo data shown in Fig. **3c** of the main text is the average of 2400 shots, and there are 122 data points in total. For these two data sets, we perform an additional reference shot after each signal shot during which the ESR or spin echo experiment is performed. The reference shots are used for normalization and consist of measuring the NV centers via SCC after preparation into either the  $m_s = 0$  or  $m_s = -1$  spin states. The preparation state is alternated between  $m_s = 0$  and  $m_s = -1$  from one from reference shot to the next. Including reference shots, the ESR data took roughly 3 hours to record. The spin echo data took roughly 11 hours. The correlation data shown in Fig. **4** of the main text do not include reference shots. Each

correlation matrix is the average of 200,000 shots and took roughly 4 hours to record.

## Charge-state readout process and fidelities

**Image processing and count integration.** As our EMCCD is not photon number-resolving, the pixel values returned by the camera upon readout are expressed as a noisy linear function of photon number in terms of analog-to-digital converter units (ADUs). In ADUs, the image features a non-zero baseline value which corresponds to zero photons. We found that this baseline value drifts over minute timescales, which can introduce spurious correlations by adding a common-mode contribution to the apparent brightness of the NV centers in an image from shot to shot. To account for this we measure the baseline value for each image by masking off a portion of the EMCCD sensor with an iris so that the masked portion receives no light. The measured baseline is then subtracted off the image and the pixel values are converted from ADUs to approximate photon number by multiplying by a fixed factor determined from the EMCCD gain specifications. To obtain the integrated counts for an NV we sum the approximate photon numbers for pixels whose centers are within a 12 pixel radius of the center of the NV.

**Thresholding.** The charge state of an NV center is inferred by thresholding on the integrated counts. The threshold is determined by fitting to a histogram of integrated counts. An example histogram and fit are shown in Extended Data Fig. 1. The fit function is a bimodal skew normal distribution of the form

$$P(C = c) = p_0 g_0(c) + p_- g_-(c) \tag{1}$$

where  $C$  is a random variable denoting the integrated counts,  $p_0$  and  $p_-$  are the probabilities that the NV was in  $NV^0$  or  $NV^-$  during the readout with  $p_0 + p_- = 1$ , and  $g_0(c)$  and  $g_-(c)$  are the individual skew normal probability density functions for the  $NV^0$  and  $NV^-$  modes respectively. Eq. (1) provides an excellent fit to the experimental data for all NV centers

studied in this work. We note that while the histogram of integrated counts is arguably described more naturally by a bimodal Poisson distribution, broadening effects are more easily captured by Eq. (1), making the bimodal skew normal distribution a better choice in practice. The threshold is determined from the fit by finding the value  $t$  that maximizes the total readout success probability

$$f_0 + f_- = P(C < t \cap NV \text{ in } NV^0) + P(C > t \cap NV \text{ in } NV^-). \quad (2)$$

For the conditional initialization experiment shown in Fig. 2 of the main text, the threshold values are decided before the experiment begins by measuring the NV centers in roughly equal mixtures of  $NV^-$  and  $NV^0$ . For the spin experiments shown in Figs. 3 and 4 of the main text, the threshold values are decided in post-processing using the histogram of integrated counts obtained from the experiments themselves.

**Fidelities.** To measure the fidelity of charge-state readout, we perform consecutive readouts without initializing or otherwise operating on the NV centers between readouts. Fidelity is then quantified by the probability that we find an NV in  $NV^0$  or  $NV^-$  given that we found the NV in the same charge state the previous two readouts. This non-destructive definition of readout fidelity reflects both the probability that the charge state is correctly determined by the final readout and the probability that the previous readout did not cause a charge-state transition. Extended Data Fig. 2 shows the charge-state readout fidelities for 50 ms (panel a) and 100 ms (panel b) exposures. The optical power for the 100 ms exposure is about half of that for the 50 ms exposure, such that the integrated counts recorded from any given NV center is nearly the same for both exposures. For the 50 ms exposure, the mean fidelity for  $NV^0$  is around 95%, while the mean fidelity for  $NV^-$  is 10 points lower, which we attribute to ionization during readout. The  $NV^0$  charge state is less susceptible to charge transitions during readout because the wavelength used for charge-state readout, 589 nm, is below the  $NV^0$  zero-phonon line. Extending the exposure to 100 ms makes readout less destructive by



reducing the rate of two-photon ionization events, which scale quadratically with intensity, leading to a marked improvement in the  $NV^-$  fidelity.

## Model for conditional charge-state initialization

Here we derive the model used to fit the experimental data shown in Fig. 2a of the main text. The model describes how the number of NV centers measured in  $NV^-$  scales with the number of initialization attempts. The model includes consideration of ionization during readout, initialization errors, and readout errors.

As a preliminary, we define readout success probability as the probability of measuring an NV in a specified charge state given that the NV was in that charge state at the beginning of the readout. With  $f_-$  and  $f_0$  denoting the readout fidelities for charge states  $NV^-$  and  $NV^0$  respectively, the following equations describing the relationship between the measured and actual numbers of NV centers in each charge state among a group of  $N$  total NV centers hold:

$$n = f_- n' + (1 - f_0)(N - n'), \quad (3)$$

$$N - n = f_0(N - n') + (1 - f_-)n'. \quad (4)$$

Here  $n$  ( $n'$ ) denotes the measured (actual) number of NV centers in  $NV^-$ . The complement  $N - n$  ( $N - n'$ ) describes the measured (actual) number of NV centers in  $NV^0$ . It is useful to write Eq. (3) as

$$n' = \frac{n - (1 - f_0)N}{(f_- + f_0 - 1)}. \quad (5)$$

The expected number of NV centers measured in  $NV^-$  after the  $i$ th initialization attempt

is

$$n_i = f_-^2 a n'_{i-1} + (1 - f_0)^2 (N - n'_{i-1}) + f_- b (N - n_{i-1}) + (1 - f_0)(1 - b)(N - n_{i-1}), \quad (6)$$

where  $n_i$  ( $n'_i$ ) describes the measured (actual) number of NV centers measured in  $NV^-$  after the  $i$ th initialization attempt,  $a$  describes the probability that an NV in  $NV^-$  is not ionized during readout, and  $b$  describes the probability that an initialization attempt on a given NV center succeeds. Eq. (6) expresses  $n_i$  as a sum of four terms: (1) the number of NV centers that were correctly determined to be in  $NV^-$  by the previous readout, were not ionized by the previous readout, and are correctly determined to be in  $NV^-$  by the current readout; (2) the number of NV centers that were incorrectly determined to be in  $NV^-$  by the previous readout and are again incorrectly determined to be in  $NV^-$  by the current readout; (3) the number of NV centers that were correctly or incorrectly determined to be in  $NV^0$  by the previous readout, were then successfully initialized into  $NV^-$ , and are correctly determined to be in  $NV^-$  by the current readout; and (4) the number of NV centers that were measured in  $NV^0$  by the previous readout, were then unsuccessfully initialized into  $NV^-$ , and are incorrectly determined to be in  $NV^-$  by the current readout.

Eq. (6) may be written in terms only of the measured values  $n_i$  and  $n_{i-1}$  using Eq. (5). After simplifying we obtain

$$n_i = c_1 n_{i-1} + c_2 N \quad (7)$$

where

$$c_1 = \frac{f_-^2 a - (1 - f_0)^2}{(f_- + f_0 - 1)} - (f_- b + (1 - f_0)(1 - b)) \quad (8)$$

$$c_2 = f_- b + (1 - f_0)(1 - b) + (1 - f_0)^2 - \frac{(1 - f_0)(f_-^2 a - (1 - f_0)^2)}{(f_- + f_0 - 1)}. \quad (9)$$

Solving the recurrence relation of Eq. (7), we arrive at a final model

$$n_i = c_1^i n_0 + c_2 N \frac{1 - c_1^i}{1 - c_1}. \quad (10)$$

We note that in the case of perfect readout fidelity ( $f_- = f_0 = 1$ ), the coefficients  $c_1$  and  $c_2$  simplify to

$$c_1 = a - b, \quad (11)$$

$$c_2 = b, \quad (12)$$

so that  $c_1 + c_2$  may be interpreted as the probability that readout does not result in ionization,  $a$ , with corrections to account for imperfect readout fidelity, and  $c_2$  may be interpreted as the initialization success probability,  $b$ , with corrections to account for imperfect readout fidelity. The fit parameters extracted from the data shown in Fig. 2a of the main text are  $n_0 = 0.66(8)$ ,  $c_1 = 0.225(15)$  and  $c_2 = 0.705(13)$ .

## Microwave sequences and fit functions for ESR and spin echo data

The microwave sequence for the ESR data shown in Fig. 3b of the main text consists of a single 64-ns microwave pulse of varying frequency. The fit function is a sum of two identical Voigt profiles with different center frequencies. Each profile is normalized such that its value at its center frequency is 1.

The microwave sequence for the spin echo data shown in Fig. 3c of the main text is a version of the typical  $\pi/2 - \tau - \pi - \tau - \pi/2$  sequence<sup>55</sup> modified to address both NV orientations under study. As in Fig. 4 of the main text, each nominal  $\pi/2$  or  $\pi$  pulse consists of a pair of separate pulses, with one pulse targeting each orientation. The pulses are delivered in series with a 16 ns buffer between them. The fit function is empirical. For NV centers 3, 6, 7, and

9, which do not display oscillations, the fit function is:

$$f(t) = b - be^{-(t/t_c)^2} - \sum_{i=1}^2 a_i e^{-((t-t_r i)/t_c)^2}. \quad (13)$$

Here  $t = 2\tau$  is the total evolution time, the  $a_i$  describe the coherence revival amplitudes,  $t_r$  describes the revival frequency, and  $t_c$  describes the coherence time of the initial collapse and each revival. The baseline value  $b$  is allowed to vary from 0.5 to account for microwave pulse errors. For NV centers 0, 1, 2, 4, 5, and 8, the revivals include a coefficient that oscillates with frequencies  $\omega_j$ :

$$f(t) = b - be^{-(t/t_c)^2} - \left( \sum_{j=1}^2 \cos(\omega_j t) \right) \sum_{i=1}^2 a_i e^{-((t-t_r i)/t_c)^2}. \quad (14)$$

## Effect of quantum projection noise on contrast of measured correlations

For the experiments described in Figs. 4c-e of the main text, we manually prepared the NV spins in either  $m_s = -1$  or  $m_s = 0$ , thereby avoiding quantum projection noise (QPN). As a result, the correlation matrices shown in Figs. 4c-e display the maximum contrast that could be measured between pairs of NV spins with our apparatus given the same experimental parameters (readout fidelities, SCC probabilities, etc.). In real applications, the correlation contrast will be reduced by QPN. The effect of QPN in the context of correlated sensing has been thoroughly studied by Rovny et al. in Ref. [5]. Here we adapt those results to obtain a simple estimate for how much QPN will reduce the correlation contrast relative to the levels shown in Fig. 4c-e. For the common case in quantum sensing where an accumulated phase  $\phi$  is mapped onto a population difference by a final  $\pi/2$  pulse before readout (such that the phase is mapped to a polar angle  $\phi + \pi/2$  in the Bloch sphere representation), the

measurable correlation between two spins is<sup>5</sup>

$$r = \langle \sin(\phi_1) \sin(\phi_2) \rangle \quad (15)$$

under ideal conditions of perfect initialization and spin-state readout, and in the absence of uncorrelated noise sources. Here  $\phi_1$  and  $\phi_2$  are the phases accumulated by the two spins due to a correlated signal. The phases are assumed to be proportional to one another and evenly distributed. The data shown in Fig. 4c-e are equivalent to the case where  $\phi_2 = \pm\phi_1$  for any pair of NV centers and  $P(\phi_1 = \pi/2) = P(\phi_1 = -\pi/2) = 0.5$  for any single NV center, leading to  $r = \pm 1$  in the ideal case. For equal phases  $\phi \equiv \phi_1 = \phi_2$  that are normally distributed with variance  $\sigma_\phi^2$ , Eq. (15) reduces to<sup>5</sup>

$$r = \frac{1}{2}(1 - e^{-2\sigma_\phi^2}). \quad (16)$$

Here  $r$  increases monotonically from 0 at  $\sigma_\phi^2 = 0$  to 0.5 for large  $\sigma_\phi^2$ . For large  $\sigma_\phi^2$  the phases are effectively uniformly distributed on  $[-\pi, \pi]$ , and therefore each individual spin is completely dephased. In this case the correlation contrast is reduced by a factor of 2 relative to the contrasts shown in Fig. 4c-e. We note that non-idealities (e.g. readout errors, initialization errors, uncorrelated noise sources) which will further reduce the correlation contrast can be captured by a prefactor that does not depend on  $r$  itself<sup>5</sup>. As such, the factor by which QPN reduces the contrast in the ideal case will reduce the contrast in the non-ideal case by the same factor for the same distribution of correlated phases.

## Effect of polarization of 589-nm light

The polarization of the 589-nm light was found to significantly affect which orientations of NV centers were visible above the background under widefield illumination. We used a polarization-maintaining fiber to couple the 589-nm light between optical tables to ensure polarization stability, and we adjusted the 589-nm polarization on the main experiment

table to optimize the count rate from just two orientations of NV centers. Extended Data Fig. 3 shows the effect of rotating the polarization of the 589-nm light. The background level is roughly constant as the polarization is rotated, but the signal level from any one NV center depends on its orientation with respect to the polarization. We suggest that all four orientations could be interrogated simultaneously by using circularly polarized excitation sources, rather than linearly polarized excitation sources.

## Animated ESR and Rabi oscillation data sets

Animated data sets showing ESR and Rabi oscillations with NV centers 0-9 are available online. The animations show the average background-subtracted EMCCD image as the microwave frequency (for ESR) or microwave pulse duration (for Rabi) is changed. The background is the average image recorded for the reference experiments where the NV centers are prepared in  $m_s = 0$ . Two versions of Rabi oscillations are shown. In the first version all 10 NV centers oscillate in phase. In the second version, NV centers of one orientation are targeted with an additional  $\pi$  pulse before SCC such that the Rabi oscillations for NV centers of different orientations are antiphase.

## Crosstalk characterization

In practice, an optical pulse which is intended to target an individual NV center or a microwave pulse which is intended to target a specific NV orientation may affect other NV centers which are not the target of the pulse. Here we discuss these crosstalk effects, focusing on the impact to spin measurements conducted using sequences similar to those shown in Figs. 2a and 3a of the main text.

**Optical crosstalk.** Focused 520-nm and 638-nm optical pulses may inadvertently affect both the charge and spin states of NV centers adjacent to a target NV. Charge-state transitions under both 520-nm and 638-nm light are two-photon processes, however, and so depend

quadratically on intensity. Therefore, crosstalk affecting the charge state is largely suppressed for optically resolved NV centers. Crosstalk affecting the spin state, on the other hand, can occur at comparably low intensities. Because spin polarization is performed globally as a separate step after charge polarization, crosstalk affecting the spin state from 520-nm charge polarization pulses is not relevant to our experiments. Crosstalk from 638-nm SCC pulses can re-polarize the spin states of nearby NV centers that have yet to undergo SCC in the sequence, thereby effectively erasing the information stored in the affected NV's spin state before it is read out. We observed this final optical crosstalk effect in practice as a reduction in the signal-to-noise ratio (SNR) of NV centers with close neighbors. This effect accounts for the slightly reduced contrast of NV 10 in Fig. 1f of the main text.

SCC crosstalk is quantified by the experiment with a single NV center shown in Extended Data Fig. 4, where an additional displaced SCC pulse is applied before an SCC pulse which is not displaced in order to simulate the effect of a nearby NV that precedes the target NV in SCC. At large displacements, the signal-to-noise ratio (SNR) approaches the value that would be obtained with no additional SCC pulse. At moderate displacements, the SNR drops as the additional SCC pulse polarizes the target NV center spin. Near zero displacement, the additional pulse performs SCC on the target NV as normal, and the subsequent SCC pulse reduces the population left in  $NV^-$  regardless of the spin state, thereby similarly reducing the contrast relative to the large-displacement limit. A Gaussian fit to the data reveals a  $1/e^2$  crosstalk radius of  $1.4(3) \mu\text{m}$ , significantly larger than the radius of a diffraction-limited 638-nm beam in our setup (about 220 nm). This indicates that NV centers which are optically resolved in EMCCD images are not necessarily sufficiently separated to be unaffected by crosstalk during SCC. The 638-nm beam radius in our apparatus may be larger than the diffraction limit as a result of wavefront errors associated with dichroics, and so the crosstalk radius could potentially be reduced by improving the beam quality. However, because spin polarization is a saturable process, the magnitude of the crosstalk effect does not scale linearly with illumination intensity. For this reason, we predict that

even with improvements to the beam quality the crosstalk radius will still be larger than the diffraction-limited beam radius.

**Microwave crosstalk.** The microwave antenna used in this work<sup>29</sup> produces fields that are homogeneous over millimeter scales, and so NV centers over a micron-scale region will experience a uniform field from a microwave pulse. To address two NV orientations we adjust the bias magnetic field to allow for frequency resolution of the  $m_s = 0 \leftrightarrow m_s = \pm 1$  transitions of the orientations. We then apply separate microwave pulses at different frequencies for each orientation. Because the pulses are delivered globally, however, NV centers of both orientations will experience the field from a microwave pulse regardless of which orientation the pulse is intended to address, which can result in undesired dynamics. Quantitatively, the amplitude of Rabi oscillations depends on the resonant frequency  $\omega_0$ , the drive frequency  $\omega_1$ , and the Rabi frequency  $\Omega$  as

$$A = \frac{\Omega^2}{(\omega_1 - \omega_0)^2 + \Omega^2}. \quad (17)$$

The AC Zeeman shift induced by an off-resonant pulse is<sup>56</sup>

$$\delta = \frac{1}{4} \Delta m_s \Omega^2 \frac{\omega_0}{\omega_0^2 - \omega_1^2} \quad (18)$$

for magnetic sublevels which differ in spin projection by  $\Delta m_s$ . The resonant frequencies of the two orientations studied in this work are 2.813 GHz (orientation A) and 2.858 GHz (orientation B), and the Rabi frequency is approximately 8 MHz for both orientations. Therefore we expect population shifts on the order of 3% and phase shifts of around 70 mrad per  $\pi$  pulse due to microwave crosstalk. Extended Data Fig. 5 shows an experiment measuring population shifts due to microwave crosstalk by applying microwave pulses to only one orientation at a time. The orientation which is not targeted by the pulse does not show a signal larger than the noise. For sensitive spin experiments which require many microwave pulses



(e.g. dynamical decoupling), experiments could be restricted to a single orientation to avoid microwave crosstalk entirely.

## Measurement speedup from parallelization

Here we calculate the speedup enabled by parallelization by estimating the amount of time various measurements would take using different measurement techniques. In particular, we will look the amount of time required to average down a signal to unit SNR for both independent and correlated spin experiments using four different techniques: (1) conventional readout with experiments on different NV centers conducted in series; (2) conventional readout with experiments on different NV centers conducted in parallel; (3) SCC readout with experiments on different NV centers conducted in series; and (4) SCC readout with experiments on different NV centers conducted in parallel. Conventional readout refers to illuminating an NV center with green light (typically 532 nm) and collecting the resultant spin state-dependent fluorescence. Because green light simultaneously repolarizes the NV spin state, the readout duration for conventional readout is limited to roughly 200 ns. Measurements with conventional readout therefore feature low measurement time overhead but also low single-shot SNR.

**Independent measurements.** The time it takes a measurement to reach unit SNR can be expressed generically for both serial and parallel independent spin experiments as

$$T = A \times (1/k)^2 \times [n (t_{o,s} + t_{i,s}) + t_{o,p} + t_{i,p}], \quad (19)$$

where  $n$  is the number of NV centers,  $t_{o,s}$  and  $t_{o,p}$  are overhead times associated with initialization and readout for serial and parallel operations respectively, and  $t_{i,s}$  and  $t_{i,p}$  are interrogation times for serial and parallel experiments respectively. The quantity  $k$  is the single-shot SNR defined as the SNR recorded for a single repetition of an experiment in which the NV center is prepared directly in either the  $m_s = 0$  or  $m_s = +/- 1$  spin state. The

single-shot SNR is typically inversely proportional to the readout noise discussed in some other works<sup>5,39</sup>. We use the single-shot SNR in our calculations here as it is easily accessed directly in experiment. The quantity  $A$  is a unitless factor that incorporates the target signal strength and additional measurement details. Realistic values for the single-shot SNR  $k$  and time variables are given in Extended Data Table 1, and the time required to reach unit SNR according to these parameters is plotted in Extended Data Fig. 6.

**Correlated measurements.** In the case of correlated measurements we examine the required measurement time to reach unit SNR for all  ${}_nC_2$  two-point correlators among  $n$  NV centers. The required measurement time can be expressed

$$T = B \times (1/k)^4 \times \binom{n}{2} (t_{o,s} + t_{i,s}). \quad (20)$$

if the correlators are measured in series using an apparatus like that developed in Ref. [5] and

$$T = B \times (1/k)^4 \times [n (t_{o,s} + t_{i,s}) + t_{o,p} + t_{i,p}]. \quad (21)$$

in the parallel case where all correlators are measured simultaneously. Here,  $B$  is a unitless factor that encodes the magnitude of the correlation due to the target signal, similar to  $A$  in Eq. (19). Note the factor of  $(1/k)^4$  in Eqs. (20) and (21)<sup>5</sup>, versus the factor of  $(1/k)^2$  in Eq. (19) for independent measurements. The results for different measurement techniques are plotted in Extended Data Fig. 7.

## Limits to scalability

In this section we discuss the limits to the scalability of our platform under conditions of improved illumination for charge-state readout by way of an SLM, light sheet, or similar approach. A key parameter determining the scalability limit is the NV density,  $d$ . For

the concrete numbers presented in this discussion we assume a diamond sample engineered to contain the maximum practical NV density as limited by the SCC crosstalk radius of 1.4  $\mu\text{m}$ . The density in this case is  $d = 0.59$  NV centers per square micron, achieved by a hexagonal packing of NV centers separated by 1.4  $\mu\text{m}$ . For reference, the NV density for the region of the diamond sample explored in this work is  $d = 0.16$  NV centers of interest per square micron. While in this work we worked with two specific NV orientations, all four NV orientations could be measured simultaneously using circularly polarized excitation sources.

**Spin relaxation and AOD bandwidth.** At elevated temperatures, spin relaxation limits the number of NV centers which can be addressed by serial operations before the spin contrast is lost. This effect is not relevant during the polarization step of our experimental sequence, as spin polarization is carried out with a global 589-nm pulse after serial charge polarization. In the SCC section of the sequence, only relaxation on the single-quantum (SQ)  $m_s = 0 \leftrightarrow m_s = \pm 1$  transitions is relevant because SCC does not discriminate between the  $m_s = \pm 1$  levels. The time constant for  $1/e$  spin contrast loss associated with SQ relaxation is  $1/(3\Omega)$  where  $\Omega$  is the SQ relaxation rate<sup>43,45</sup>. At room temperature, this time constant is around 5 ms for NV centers in bulk diamond<sup>42</sup>. For near-surface NV centers, accelerated SQ relaxation causes  $1/e$  contrast loss within a few milliseconds for shallow NV centers<sup>43</sup> and within roughly a single millisecond for NV centers in nanodiamonds<sup>45</sup>. The duration of each SCC operation is dominated by the access time required to effectively update the RF frequencies at the AOD to reposition the 638-nm beam. The AODs used in this work both have nominal access times of  $\tau = 10 \mu\text{s}$  for beams that fill the AODs'  $7 \times 7$  mm apertures. The maximum number of NV centers that can be addressed by serial SCC before  $1/e$  contrast loss is

$$\max n = \frac{1}{3\Omega\tau} \quad (\text{relaxation-limited}) \quad (22)$$

where  $n$  is the number of NV centers measured in parallel. For an aperture-filling beam

Eq. (22) evaluates to 500 NV centers in the bulk context, around 300 NV centers in the shallow context, and around 100 NV centers in the nanodiamond context at room temperature.

The spin relaxation limit to  $n$  may be increased by reducing the access time of the AOD. The access time is set by the time required for the RF sound wave in the AOD to traverse the beam front, so the access time may be reduced by reducing the beam size. Reducing the beam size at the AOD while maintaining the beam size and angular bandwidth at the back aperture of the objective (by adjusting the lenses in the 4f configuration) would require a corresponding increase in usage of the AOD’s RF bandwidth. We only needed 2.4 MHz (2.9 MHz) of RF bandwidth out of the available 40 MHz (45 MHz) for the 638-nm (520-nm) AOD along either of the  $xy$ -axes to span the roughly  $8 \times 8 \mu\text{m}$  region examined in this work. Therefore, by exchanging the AOD’s “field of view” for improved access times, we can optimize the maximum of NV centers in the spin relaxation-limited regime. The AOD bandwidth limit to  $n$  can be expressed

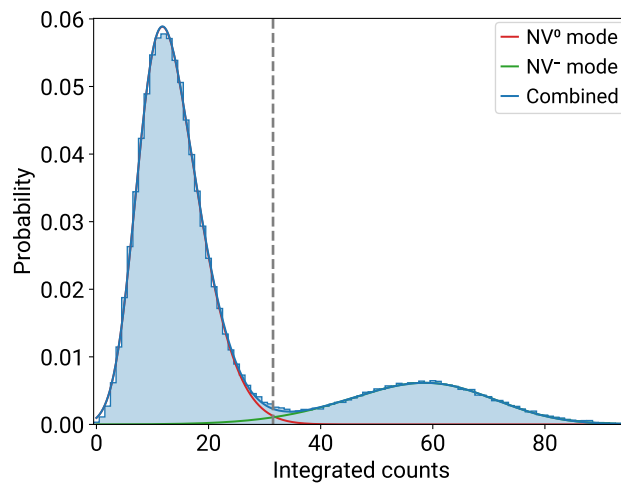
$$\max n = d \times \left( \frac{\partial x}{\partial f} \delta f \right)^2 \quad (\text{AOD bandwidth-limited}) \quad (23)$$

where  $x$  is the beam position,  $f$  is the RF frequency, and  $\delta f$  is the RF bandwidth. We assume a linear relation between the beam position and the RF frequency over the full RF bandwidth range, and we take  $\partial x/\partial f$  to be the values observed empirically in this work:  $3.33 \mu\text{m}/\text{MHz}$  for the 638-nm AOD and  $2.76 \mu\text{m}/\text{MHz}$  for the 520-nm AOD for aperture-filling beams. The 638-nm (520-nm) AOD therefore has an effective field of view of  $0.13 \times 0.13 \text{ mm}$  ( $0.12 \times 0.12 \text{ mm}$ ). Note that we treat the  $x$ - and  $y$ -channels of the AODs independently here such that the AOD bandwidth-limited sample area is square. Both the access time  $\tau$  and the conversion factor between beam position and RF frequency  $\partial x/\partial f$  scale approximately linearly with the beam size, leading to an optimum beam size that allows the most NV centers to be interrogated in parallel for a given SQ relaxation rate. The result of this tradeoff is illustrated in Extended Data Fig. 8. The intersection points

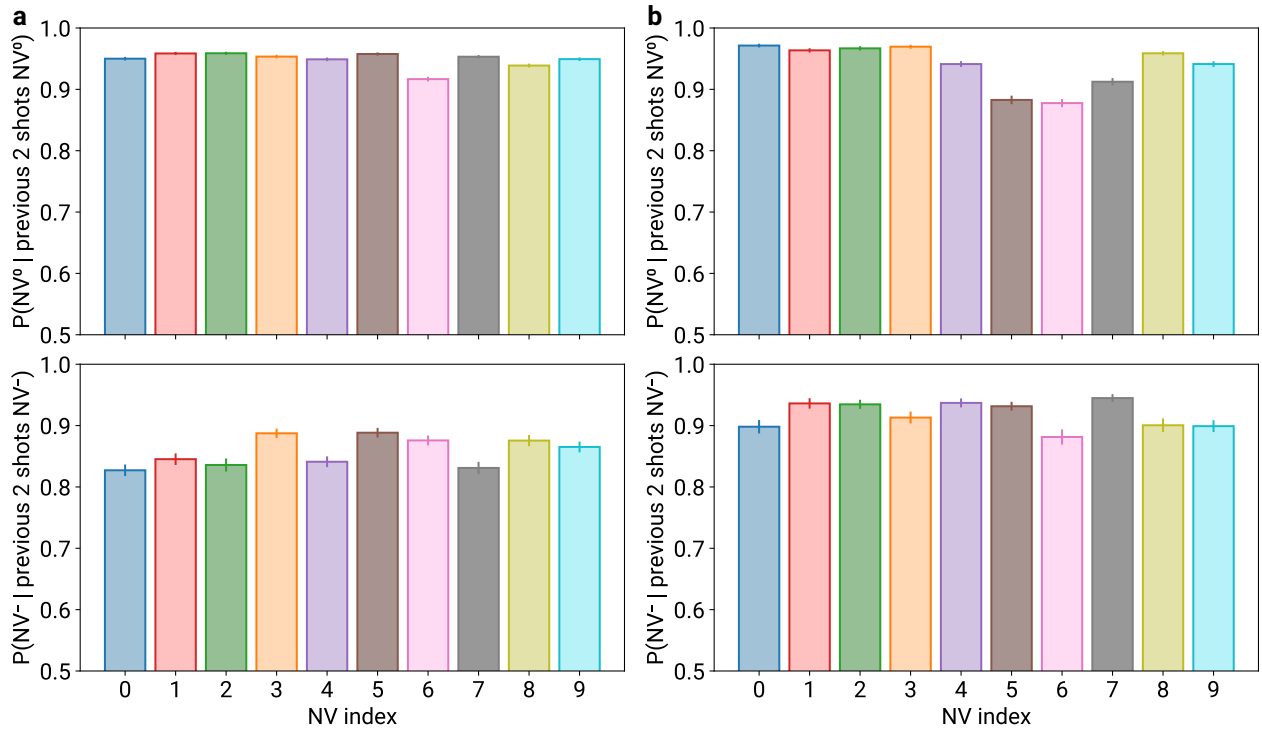
between the AOD bandwidth-limited curve and the spin relaxation-limited curves represent the optimum beam size and the maximum number of NVs achievable for each context. From this, the maximum  $n$  is 1100 in the bulk context, 800 in the shallow context, and 400 in the nanodiamond context given the hardware used in this work. We note that for millimeter-scale beams neither the peak diffraction efficiency nor the RF bandwidth is likely to be significantly affected by a reduction in beam size<sup>57</sup>. Small changes in diffraction efficiency that do occur could be compensated for by increasing the RF or laser powers, as the optical powers required for serial operations are relatively low. Another approach to increasing access times is to use an AOD that features a higher speed of sound. Because a higher speed of sound dictates a smaller angular bandwidth for the same RF bandwidth, this approach would similarly require using more of the available RF bandwidth to scan a region of the same area in the sample.

**Beyond spin relaxation.** At cryogenic temperatures the NV spin lifetime can exceed 10 seconds<sup>46</sup>. In this regime spin relaxation is not a limiting factor ( $\max n = 10^6$ ) and so the 638-nm and 520-nm beams should fill the AOD apertures to maximize angular bandwidth, resulting in a limit of around 9,100 NV centers (Extended Data Fig. 8). Other potentially limiting factors include the objective field of view, the resolution of the EMCCD camera, the available optical power for parallel operations with 589-nm light, and the potential limits of the specific 589-nm illumination method. The field of view of the objective used in this work is 0.265 mm in diameter, 40% larger than the diagonal size of the AOD field of view. The EMCCD camera used in this work has a resolution of  $512 \times 512$  pixels. If the diffraction-limited spot for a single NV center (around 500 nm in diameter given our microscope objective) is mapped to a 2 pixel diameter on the camera pixel array, then the total field of view of the camera is  $0.13 \times 0.13$  mm, slightly larger than the bandwidth limit for the 520-nm AOD. The 589-nm intensity required in this work was less than  $100 \text{ W/cm}^2$ . At this intensity, a  $0.3 \text{ mm}^2$  region could be uniformly illuminated with just 100 mW of optical power. While different illumination methods will require more or less optical power

to achieve the same effect, this calculation indicates that the availability of 589-nm optical power is not a significant limit to scalability. Light sheet illumination will not introduce other potential limiting factors to consider. Illumination with an array of focused spots would require a DMD or SLM with a suitably high resolution. We note that SLMs have already been used to generate optical tweezer arrays with over 12,000 sites<sup>58</sup>. We conclude that the upper limit of scalability for our platform is around 9,100 NV centers with hardware similar to that used in this work, and that the limiting factor is AOD bandwidth.

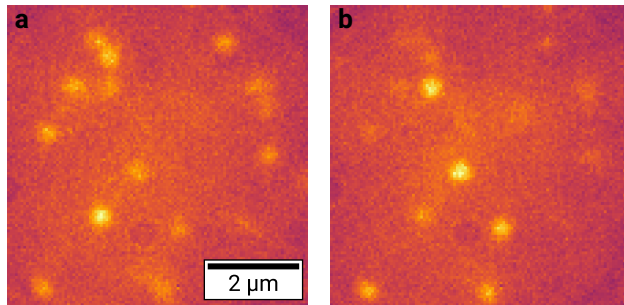


**Extended Data Fig. 1 | Charge-state readout threshold determination.** Histogram of integrated counts for the data set shown in Fig. 4c in the main text for NV 0. The histogram is fit to a bimodal distribution constructed from two skew normal distributions. The contribution to the total fit from each mode is shown in red and green, and the combined fit is shown in blue. Grey dashed line shows the threshold value extracted from the fit.

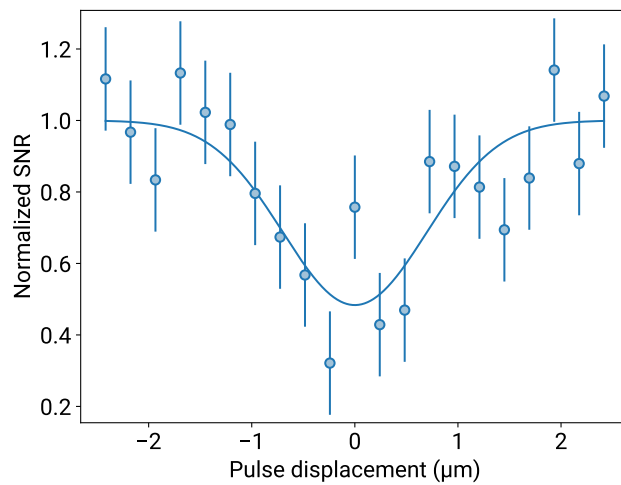


**Extended Data Fig. 2 | Charge-state readout fidelities characterized by consecutive readout.** Plots show the probability of measuring an NV in  $NV^0$  (top panels) or  $NV^-$  (bottom panels) given that the NV was measured in the same charge state for the previous two readouts. **a**, 50-ms exposure. **b**, 100-ms exposure.

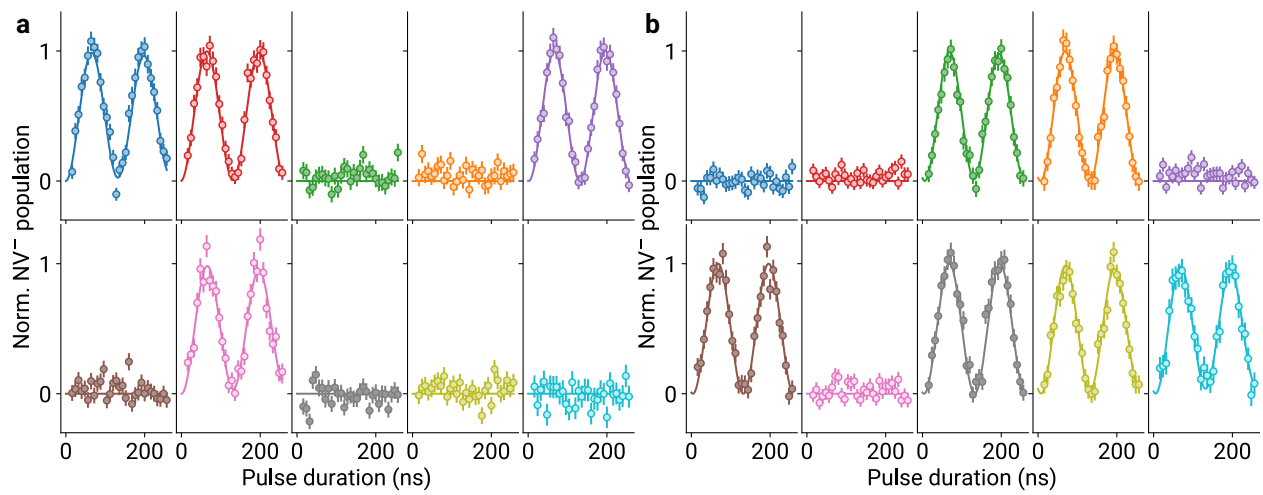




**Extended Data Fig. 3 | Effect of rotating linear polarization of 589-nm light on widefield images.** **a**, Widefield image taken with the 589-nm polarization used for experiments shown in main text. **b**, Widefield image taken with the 589-nm polarization rotated by approximately 80 degrees with respect to the polarization in **a**.



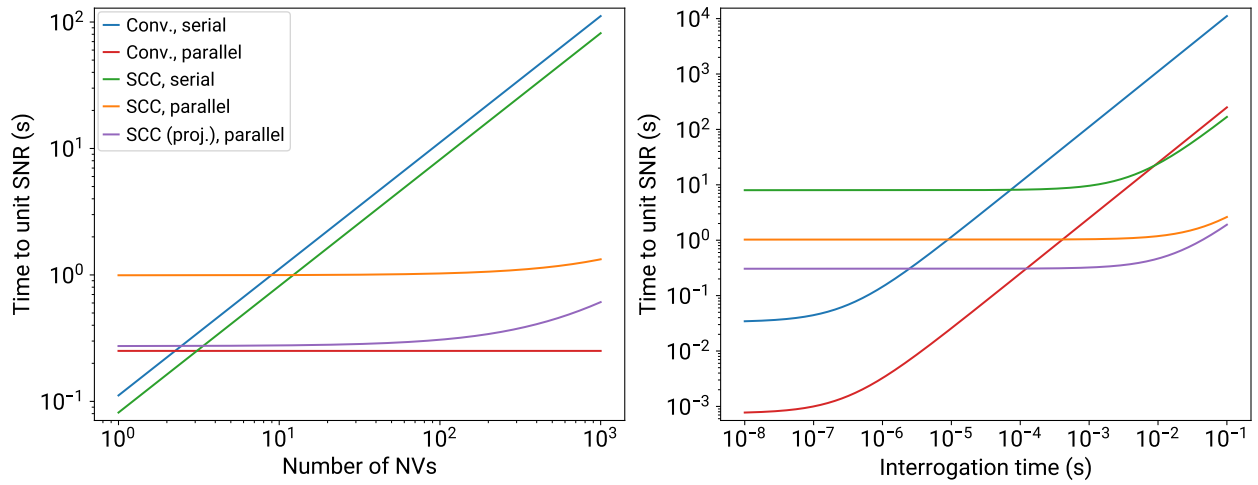
**Extended Data Fig. 4 | SCC crosstalk characterization.** The signal-to-noise ratio (SNR) of an NV spin is measured with two SCC pulses applied. The first pulse is displaced relative to the center of the NV. The second pulse is not displaced. Solid line is a Gaussian fit to the data. The SNR values are normalized to the asymptotic value of the fit. Error bars are one standard error.



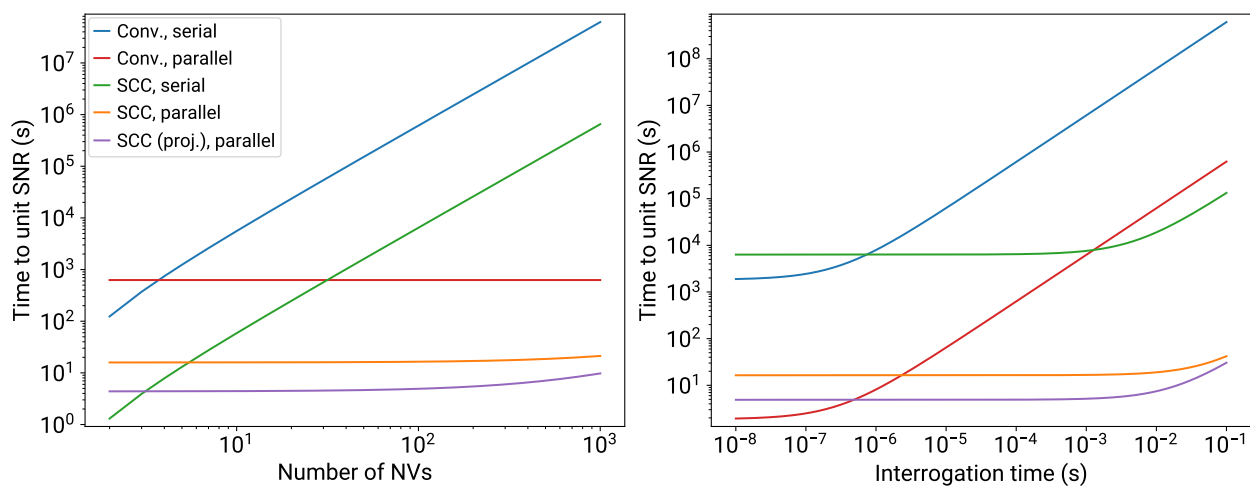
**Extended Data Fig. 5 | Microwave crosstalk characterization.** Measurements show Rabi oscillation where a single microwave tone is applied to selectively target one orientation. **a**, Orientation A. **b**, Orientation B.

Readout mode	Series/ parallel	$k$	$t_{o,s}$ (s)	$t_{i,s}$ (s)	$t_{o,p}$ (s)	$t_{i,p}$ (s)
conv.	series	0.03	$0.3 \times 10^{-6}$	variable	0	0
conv.	parallel	0.02	0	0	$0.3 \times 10^{-6}$	variable
SCC	series	0.25	$5 \times 10^{-3}$	variable	0	0
SCC	parallel	0.25	$21 \times 10^{-6}$	0	$62 \times 10^{-3}$	variable
SCC (proj.)	parallel	0.25	$21 \times 10^{-6}$	0	$17 \times 10^{-3}$	variable

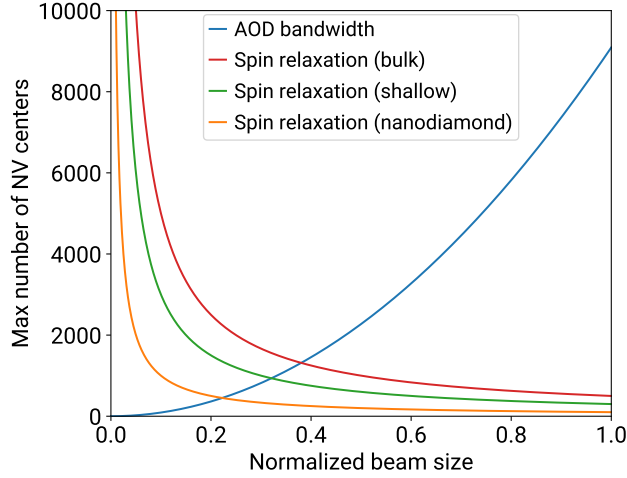
**Extended Data Table 1 | Variables that determine the time it takes to reach unit SNR for different spin measurement techniques.** For conventional readout we assume a 300 ns overhead for readout and polarization. For parallel conventional readout the SNR is reduced to account for the fact that current scientific cameras cannot be gated on  $\sim 100$  ns timescales and so would need to be continuously exposed during the entire green illumination, rather than only during the window that maximizes SNR. For parallel SCC measurements we assume a dead time of 12 ms per shot for camera readout. The values of  $k$  achieved in this work are between 0.2 and 0.3. The final row features the projected scenario where single-shot charge-state readout is achieved with a 5 ms exposure using a spatial light modulator (SLM) or similar device.



**Extended Data Fig. 6 | Time to resolve signals for independent spin measurements using different measurement techniques.** The plots show the amount of time it takes to reach unit SNR according to Eq. (19) for the techniques described in Table 1. **a**, Required measurement time vs number of NV centers with  $A = 1$  and an interrogation time of  $100 \mu\text{s}$ , a realistic  $T_2$  coherence time for a shallow NV center<sup>59</sup>. **b**, Required measurement time vs interrogation time with  $A = 1$  and  $n = 100$  NV centers.



**Extended Data Fig. 7 | Time to resolve all possible two-point correlators using different measurement techniques.** The plots show the amount of time it takes to reach unit SNR for the techniques described in Table 1, according to Eq. (20) for the serial techniques and Eq. (21) for the parallel techniques. **a**, Required measurement time vs number of NV centers with  $B = 1$  and an interrogation time of 100  $\mu$ s. **b**, Required measurement time vs interrogation time with  $B = 1$  and  $n = 100$  NV centers.



**Extended Data Fig. 8 | Limits to scalability for different limiting factors.** The maximum number of NV centers that may be interrogated in parallel depends inversely on the beam size in the spin relaxation-limited case (red, green, and orange curves calculated from Eq. (22)) and quadratically on the beam size in the AOD bandwidth-limited case (blue curve calculated from Eq. (23) for the 520-nm AOD). The beam size is normalized to the size of the AOD aperture. The intersection points of the curves indicate the optimum beam size and maximum number of NV centers for different SQ relaxation lifetimes. We assume  $1/(3\Omega) = 5$  ms for NV centers deep in bulk diamond,  $1/(3\Omega) = 3$  ms for shallow NV centers, and  $1/(3\Omega) = 1$  ms for NV centers in nanodiamonds. At low temperatures, scalability is limited by the AOD bandwidth to around 9,100 NV centers.

## References

1. Levine, E. V., Turner, M. J., Kehayias, P., Hart, C. A., Langellier, N., Trubko, R., Glenn, D. R., Fu, R. R. & Walsworth, R. L. Principles and techniques of the quantum diamond microscope. *Nanophotonics* **8**, 1945–1973 (2019).
2. Segawa, T. F. & Igarashi, R. Nanoscale quantum sensing with nitrogen-vacancy centers in nanodiamonds – A magnetic resonance perspective. *Progress in Nuclear Magnetic Resonance Spectroscopy* **134**, 20–38 (2023).
3. Abobeih, M. H., Wang, Y., Randall, J., Loenen, S., Bradley, C. E., Markham, M., Twitchen, D. J., Terhal, B. M. & Taminiou, T. H. Fault-tolerant operation of a logical qubit in a diamond quantum processor. *Nature* **606**, 884–889 (2022).
4. Fung, F., Rosenfeld, E., Schaefer, J., Kabcenell, A., Gieseler, J., Zhou, T., Madhavan, T., Aslam, N., Yacoby, A. & Lukin, M. Toward programmable quantum processors based on spin qubits with mechanically mediated interactions and transport. *Physical Review Letters* **132**, 263602 (2024).
5. Rovny, J., Yuan, Z., Fitzpatrick, M., Abdalla, A. I., Futamura, L., Fox, C., Cambria, M. C., Kolkowitz, S. & de Leon, N. P. Nanoscale covariance magnetometry with diamond quantum sensors. *Science* **378**, 1301–1305 (2022).
6. Ji, W., Liu, Z., Guo, Y., Hu, Z., Zhou, J., Dai, S., Chen, Y., Yu, P., Wang, M., Xia, K., *et al.* Correlated sensing with a solid-state quantum multisensor system for atomic-scale structural analysis. *Nature Photonics* **18**, 230–235 (2024).
7. Delord, T., Monge, R. & Meriles, C. A. Correlated spectroscopy of electric noise with color center clusters. *Nano Letters* (2024).
8. Huxter, W. S., Dalmagioni, F. & Degen, C. L. Multiplexed scanning microscopy with dual-qubit spin sensors. *arXiv preprint arXiv:2407.19576* (2024).



9. Maze, J. R., Stanwix, P. L., Hodges, J. S., Hong, S., Taylor, J. M., Cappellaro, P., Jiang, L., Dutt, M. G., Togan, E., Zibrov, A., *et al.* Nanoscale magnetic sensing with an individual electronic spin in diamond. *Nature* **455**, 644–647 (2008).
10. Dolde, F., Fedder, H., Doherty, M. W., Nöbauer, T., Rempp, F., Balasubramanian, G., Wolf, T., Reinhard, F., Hollenberg, L. C., Jelezko, F., *et al.* Electric-field sensing using single diamond spins. *Nature Physics* **7**, 459–463 (2011).
11. Rondin, L., Tetienne, J.-P., Spinicelli, P., Dal Savio, C., Karrai, K., Dantelle, G., Thivaille, A., Rohart, S., Roch, J.-F. & Jacques, V. Nanoscale magnetic field mapping with a single spin scanning probe magnetometer. *Applied Physics Letters* **100** (2012).
12. Dutt, M. G., Childress, L., Jiang, L., Togan, E., Maze, J., Jelezko, F., Zibrov, A., Hemmer, P. & Lukin, M. Quantum register based on individual electronic and nuclear spin qubits in diamond. *Science* **316**, 1312–1316 (2007).
13. Bernien, H., Hensen, B., Pfaff, W., Koolstra, G., Blok, M. S., Robledo, L., Tamirniau, T. H., Markham, M., Twitchen, D. J., Childress, L., *et al.* Heralded entanglement between solid-state qubits separated by three metres. *Nature* **497**, 86–90 (2013).
14. Balasubramanian, G., Neumann, P., Twitchen, D., Markham, M., Kolesov, R., Mizuochi, N., Isoya, J., Achard, J., Beck, J., Tissler, J., *et al.* Ultralong spin coherence time in isotopically engineered diamond. *Nature materials* **8**, 383–387 (2009).
15. Herbschleb, E., Kato, H., Maruyama, Y., Danjo, T., Makino, T., Yamasaki, S., Ohki, I., Hayashi, K., Morishita, H., Fujiwara, M., *et al.* Ultra-long coherence times amongst room-temperature solid-state spins. *Nature communications* **10**, 3766 (2019).
16. Vool, U., Hamo, A., Varnavides, G., Wang, Y., Zhou, T. X., Kumar, N., Dovzhenko, Y., Qiu, Z., Garcia, C. A., Pierce, A. T., *et al.* Imaging phonon-mediated hydrodynamic flow in WTe<sub>2</sub>. *Nature Physics* **17**, 1216–1220 (2021).

17. Huang, M., Sun, Z., Yan, G., Xie, H., Agarwal, N., Ye, G., Sung, S. H., Lu, H., Zhou, J., Yan, S., *et al.* Revealing intrinsic domains and fluctuations of moiré magnetism by a wide-field quantum microscope. *Nature Communications* **14**, 5259 (2023).
18. Bhattacharyya, P., Chen, W., Huang, X., Chatterjee, S., Huang, B., Kobrin, B., Lyu, Y., Smart, T., Block, M., Wang, E., *et al.* Imaging the Meissner effect in hydride superconductors using quantum sensors. *Nature* **627**, 73–79 (2024).
19. Choi, J., Zhou, H., Landig, R., Wu, H.-Y., Yu, X., Von Stetina, S. E., Kucsko, G., Mango, S. E., Needleman, D. J., Samuel, A. D., *et al.* Probing and manipulating embryogenesis via nanoscale thermometry and temperature control. *Proceedings of the National Academy of Sciences* **117**, 14636–14641 (2020).
20. Nie, L., Nusantara, A., Damle, V., Sharmin, R., Evans, E., Hemelaar, S., Van der Laan, K., Li, R., Perona Martinez, F., Vedelaar, T., *et al.* Quantum monitoring of cellular metabolic activities in single mitochondria. *Science advances* **7**, eabf0573 (2021).
21. Abendroth, J. M., Herb, K., Janitz, E., Zhu, T., Völker, L. A. & Degen, C. L. Single-nitrogen–vacancy NMR of amine-functionalized diamond surfaces. *Nano Letters* **22**, 7294–7303 (2022).
22. Liu, K. S., Henning, A., Heindl, M. W., Allert, R. D., Bartl, J. D., Sharp, I. D., Rizzato, R. & Bucher, D. B. Surface NMR using quantum sensors in diamond. *Proceedings of the National Academy of Sciences* **119**, e2111607119 (2022).
23. Ariyaratne, A., Bluvstein, D., Myers, B. A. & Jayich, A. C. B. Nanoscale electrical conductivity imaging using a nitrogen-vacancy center in diamond. *Nature communications* **9**, 2406 (2018).
24. Finco, A., Haykal, A., Tanos, R., Fabre, F., Chouaieb, S., Akhtar, W., Robert-Philip, I., Legrand, W., Ajejas, F., Bouzehouane, K., *et al.* Imaging non-collinear antiferromagnetic textures via single spin relaxometry. *Nature communications* **12**, 767 (2021).

25. Glenn, D. R., Bucher, D. B., Lee, J., Lukin, M. D., Park, H. & Walsworth, R. L. High-resolution magnetic resonance spectroscopy using a solid-state spin sensor. *Nature* **555**, 351–354 (2018).
26. Ziffer, M. E., Machado, F., Ursprung, B., Lozovoi, A., Tazi, A. B., Yuan, Z., Ziebel, M. E., Delord, T., Zeng, N., Telford, E., *et al.* Quantum noise spectroscopy of critical slowing down in an atomically thin magnet. *arXiv preprint arXiv:2407.05614* (2024).
27. Scholten, S., Healey, A., Robertson, I., Abrahams, G., Broadway, D. & Tetienne, J.-P. Widefield quantum microscopy with nitrogen-vacancy centers in diamond: Strengths, limitations, and prospects. *Journal of Applied Physics* **130** (2021).
28. Kaufman, A. M. & Ni, K.-K. Quantum science with optical tweezer arrays of ultracold atoms and molecules. *Nature Physics* **17**, 1324–1333 (2021).
29. Sasaki, K., Monnai, Y., Saijo, S., Fujita, R., Watanabe, H., Ishi-Hayase, J., Itoh, K. M. & Abe, E. Broadband, large-area microwave antenna for optically detected magnetic resonance of nitrogen-vacancy centers in diamond. *Review of Scientific Instruments* **87** (2016).
30. Aslam, N., Waldherr, G., Neumann, P., Jelezko, F. & Wrachtrup, J. Photo-induced ionization dynamics of the nitrogen vacancy defect in diamond investigated by single-shot charge state detection. *New Journal of Physics* **15**, 013064 (2013).
31. Wirtitsch, D., Wachter, G., Reisenbauer, S., Gulka, M., Ivády, V., Jelezko, F., Gali, A., Nesladek, M. & Trupke, M. Exploiting ionization dynamics in the nitrogen vacancy center for rapid, high-contrast spin, and charge state initialization. *Physical Review Research* **5**, 013014 (2023).
32. Shields, B. J., Unterreithmeier, Q. P., de Leon, N. P., Park, H. & Lukin, M. D. Efficient readout of a single spin state in diamond via spin-to-charge conversion. *Physical review letters* **114**, 136402 (2015).

33. Endres, M., Bernien, H., Keesling, A., Levine, H., Anschuetz, E. R., Krajenbrink, A., Senko, C., Vuletic, V., Greiner, M. & Lukin, M. D. Atom-by-atom assembly of defect-free one-dimensional cold atom arrays. *Science* **354**, 1024–1027 (2016).
34. Barredo, D., De Léséleuc, S., Lienhard, V., Lahaye, T. & Browaeys, A. An atom-by-atom assembler of defect-free arbitrary two-dimensional atomic arrays. *Science* **354**, 1021–1023 (2016).
35. Kim, H., Lee, W., Lee, H.-g., Jo, H., Song, Y. & Ahn, J. In situ single-atom array synthesis using dynamic holographic optical tweezers. *Nature communications* **7**, 13317 (2016).
36. Smeltzer, B., Childress, L. & Gali, A.  $^{13}\text{C}$  hyperfine interactions in the nitrogen-vacancy centre in diamond. *New Journal of Physics* **13**, 025021 (2011).
37. Cujia, K. S., Herb, K., Zopes, J., Abendroth, J. M. & Degen, C. L. Parallel detection and spatial mapping of large nuclear spin clusters. *Nature Communications* **13**, 1260 (2022).
38. Van de Stolpe, G., Kwiatkowski, D., Bradley, C., Randall, J., Abobeih, M., Breitweiser, S., Bassett, L., Markham, M., Twitchen, D. & Taminiau, T. Mapping a 50-spin-qubit network through correlated sensing. *Nature Communications* **15**, 2006 (2024).
39. Degen, C. L., Reinhard, F. & Cappellaro, P. Quantum sensing. *Reviews of modern physics* **89**, 035002 (2017).
40. Stelzer, E. H., Strobl, F., Chang, B.-J., Preusser, F., Preibisch, S., McDole, K. & Fiolka, R. Light sheet fluorescence microscopy. *Nature Reviews Methods Primers* **1**, 73 (2021).
41. Ohno, K., Joseph Heremans, F., Bassett, L. C., Myers, B. A., Toyli, D. M., Bleszynski Jayich, A. C., Palmstrøm, C. J. & Awschalom, D. D. Engineering shallow spins in diamond with nitrogen delta-doping. *Applied Physics Letters* **101** (2012).

42. Cambria, M., Gardill, A., Li, Y., Norambuena, A., Maze, J. & Kolkowitz, S. State-dependent phonon-limited spin relaxation of nitrogen-vacancy centers. *Physical Review Research* **3**, 013123 (2021).
43. Myers, B. A., Ariyaratne, A. & Jayich, A. B. Double-quantum spin-relaxation limits to coherence of near-surface nitrogen-vacancy centers. *Physical review letters* **118**, 197201 (2017).
44. Sangtawesin, S., Dwyer, B. L., Srinivasan, S., Allred, J. J., Rodgers, L. V., De Greve, K., Stacey, A., Dontschuk, N., O'Donnell, K. M., Hu, D., *et al.* Origins of diamond surface noise probed by correlating single-spin measurements with surface spectroscopy. *Physical Review X* **9**, 031052 (2019).
45. Gardill, A., Cambria, M. C. & Kolkowitz, S. Fast relaxation on qutrit transitions of nitrogen-vacancy centers in nanodiamonds. *Physical Review Applied* **13**, 034010 (2020).
46. Cambria, M., Norambuena, A., Dinani, H., Thiering, G., Gardill, A., Kemeny, I., Li, Y., Lordi, V., Gali, Á., Maze, J., *et al.* Temperature-dependent spin-lattice relaxation of the nitrogen-vacancy spin triplet in diamond. *Physical Review Letters* **130**, 256903 (2023).
47. Robledo, L., Childress, L., Bernien, H., Hensen, B., Alkemade, P. F. & Hanson, R. High-fidelity projective read-out of a solid-state spin quantum register. *Nature* **477**, 574–578 (2011).
48. Irber, D. M., Poggiali, F., Kong, F., Kieschnick, M., Lüthmann, T., Kwiatkowski, D., Meijer, J., Du, J., Shi, F. & Reinhard, F. Robust all-optical single-shot readout of nitrogen-vacancy centers in diamond. *Nature Communications* **12**, 532 (2021).
49. Zhang, Q., Guo, Y., Ji, W., Wang, M., Yin, J., Kong, F., Lin, Y., Yin, C., Shi, F., Wang, Y., *et al.* High-fidelity single-shot readout of single electron spin in diamond with spin-to-charge conversion. *Nature communications* **12**, 1529 (2021).

50. Rovny, J., Gopalakrishnan, S., Jayich, A. C. B., Maletinsky, P., Demler, E. & de Leon, N. P. New opportunities in condensed matter physics for nanoscale quantum sensors. *arXiv preprint arXiv:2403.13710* (2024).
51. Du, J., Shi, F., Kong, X., Jelezko, F. & Wrachtrup, J. Single-molecule scale magnetic resonance spectroscopy using quantum diamond sensors. *Reviews of Modern Physics* **96**, 025001 (2024).
52. Awschalom, D. D., Hanson, R., Wrachtrup, J. & Zhou, B. B. Quantum technologies with optically interfaced solid-state spins. *Nature Photonics* **12**, 516–527 (2018).
53. Bradley, C. E., Randall, J., Aboobeih, M. H., Berrevoets, R. C., Degen, M. J., Bakker, M. A., Markham, M., Twitchen, D. J. & Taminiau, T. H. A ten-qubit solid-state spin register with quantum memory up to one minute. *Physical Review X* **9**, 031045 (2019).
54. Cheng, K.-H., Kazi, Z., Rovny, J., Zhang, B., Nassar, L., Thompson, J. D. & de Leon, N. P. Massively multiplexed nanoscale magnetometry with diamond quantum sensors. *arXiv preprint arXiv:2408.11666* (2024).
55. Childress, L., Gurudev Dutt, M., Taylor, J., Zibrov, A., Jelezko, F., Wrachtrup, J., Hemmer, P. & Lukin, M. Coherent dynamics of coupled electron and nuclear spin qubits in diamond. *Science* **314**, 281–285 (2006).
56. Ruster, T., Kaufmann, H., Luda, M. A., Kaushal, V., Schmiegelow, C. T., Schmidt-Kaler, F. & Poschinger, U. Entanglement-based dc magnetometry with separated ions. *Physical Review X* **7**, 031050 (2017).
57. Chang, I. Acousto-optic devices and applications. *Handbook of optics* **2**, 12–1 (1995).
58. Manetsch, H. J., Nomura, G., Bataille, E., Leung, K. H., Lv, X. & Endres, M. A tweezer array with 6100 highly coherent atomic qubits. *arXiv preprint arXiv:2403.12021* (2024).
59. Wang, J., Zhang, W., Zhang, J., You, J., Li, Y., Guo, G., Feng, F., Song, X., Lou, L., Zhu, W., *et al.* Coherence times of precise depth controlled NV centers in diamond. *Nanoscale* **8**, 5780–5785 (2016).